# A numerical viscoelastic model of ground response assimilating pore-water pressure measurements

S.P. Oliveira[1], J.S. Azevedo[2] and M.J. Porsani[3]

[1] INCT-GP, DMAT and PPGG, Universidade Federal do Paraná, Curitiba, Brazil

[2] CETEC, Universidade Federal do Recôncavo da Bahia, Cruz das Almas, Brazil

[3] INCT-GP and IGEO, Universidade Federal da Bahia, Salvador, Brazil

ABSTRACT    We consider a simple one-dimensional, viscoelastic model for shear-wave propagation on liquefiable soils. The soil is modelled as a layered medium parametrized by shear modulus and viscosity, which in turn depend on the excess pore-water pressure ratio. We numerically solve the resulting wave propagation model with the spectral element method, and employ simulated annealing and weighted Gauss-Newton inversion algorithms to minimize the misfit of surface displacement, velocity, and acceleration. This procedure is validated using recorded ground motion and pore-water pressure data from the Imperial Valley Wildlife and the Garner Valley downhole arrays. Parameter inversion is also carried out with linear models with constant shear modulus and viscosity, and the proposed model provides better fitness in the presence of strong motion, especially in the 1987 Superstition Hills earthquake.

## 1. Introduction

A topic of great interest in seismic behaviour of soil is the ability to model physical properties associated with large strains, in particular local changes of soil properties resulting from earthquake strong motion. The validity of the models depends on the detailed documentation of seismic events, such as the 1987 Superstition Hills earthquake at the Wildlife Site, California. This event is particularly challenging due to the loss of soil stiffness during liquefaction (Holzer and Youd, 2007).

The wave equation in one-dimensional, layered media with a prescribed (shear) stress-strain model is a common mathematical framework for site response analysis, though 2D and 3D methods are available (Du and Wang, 2015; Montoya-Noguera and Lopez-Caballero, 2016; Fayun *et al.,* 2017). In general, one has to seek a balance between accuracy and complexity when choosing from linear, equivalent linear, or nonlinear models. For instance, Ching and Glaser (2001) found, from numerical experiments with vertical array data from Garner Valley and Wildlife Site, that linear predictions were as accurate as nonlinear, except under soil liquefaction. In this sense, the ranges of ground motions over which each type of model is accurate (Kaklamanos *et al.*, 2015) are useful to decide which stress-strain model to use. On the other hand, the comparison between different nonlinear models may be a difficult task; the combined effort of several research groups has led to contributions in this direction (Régnier *et al.,* 2016, 2018).

The stress-strain relation has long been recognized as a critical soil property (Hardin and Drnevich, 1972), but recent studies have emphasized the importance of pore-pressure effects as well. Montoya-Noguera and Lopez-Caballero (2016) verified that models that do not include coupling of excess pore pressure will predict higher surface accelerations. Oral *et al.* (2017) noted that, in the absence of pore-pressure effects, even nonlinear models overestimate high-frequency motion and underestimate amplification of low frequencies. Groholski *et al.* (2014) reproduced the measured motions and excess pore-water pressures under total stress conditions from downhole arrays behaviour by means of a self-learning inverse analysis algorithm.

We introduce an improved linear model where pore-water pressure is incorporated as input data. The dependence of pore pressure is provided by a relationship between shear modulus and excess pore-water pressure ratio (Matasovic and Vucetic, 1993; Groholski *et al.,* 2014). Moreover, we assume the viscous damping coefficient depends on shear modulus. The resulting model has time-dependent coefficients whose time history is driven by pore pressure records. This approach profits from the availability of pore-water pressure data in some geotechnical field sites, such as the ones maintained by the Network for Earthquake Engineering Simulation [NEES, see, e.g. Chandra *et al*. (2015)]. With this approach, we aim to extend the applicability of the linear model for stronger ground motions, providing a better response to events where liquefaction takes place. Up to date, such a phenomenon can only be handled with nonlinear models.

Among the several numerical methods available to simulate linear and nonlinear models, such as the Goupillaud method (Ching and Glaser, 2001), finite differences (Bonilla *et al.*, 2005) and finite elements (Montoya-Noguera and Lopez-Caballero, 2016; Fayun *et al.*, 2017), we have chosen to discretize the proposed model with the spectral element method (SEM) with Chebyshev collocation points (Seriani and Priolo, 1994). Although SEM is usually employed for seismic wave propagation on regional and global scales (Faccioli *et al.*, 1997; Komatitsch and Tromp, 2002; Stupazzini *et al.*, 2009), it has been recently employed in the study of seismic response analysis (Du and Wang, 2015; Oral *et al.*, 2017). The model is formulated in time domain and temporal discretization is carried out with the average acceleration Newmark method (Hughes, 1987).

The Newmark scheme naturally provides approximations for not only displacement but also velocity and acceleration, which motivates an inversion strategy to minimize the misfit of three-component (Oral *et al.*, 2017) surface data. The target parameters are viscosity and stiffness modulus at each layer, in addition to time scale factors that are employed to estimate pore pressure where measurements are not available. As in Mercado *et al.* (2015), the parameter identification is formulated as a nonlinear least squares problem. We use the very fast simulated annealing (Ingber, 1989; Sen and Stoffa, 2013) followed by weighted Gauss-Newton (WGN) iterations (Porsani *et al.*, 2001; Porsani and Oliveira, 2008).

We employ the proposed methodology in the *M* 6.6 Superstition Hills earthquake of 24 November 1987 (Brady *et al.*, 1989) and the *M* 5.4 Southern California earthquake of 7 July 2010 (U.S. Geological Survey, 2010). For Superstition Hills, we consider the data from the former Wildlife Liquefaction Array (Brady *et al.*, 1989) and the layered model proposed in Bonilla *et al.* (2005), whereas for the Southern California earthquake, we take into account the NEES Garney Valley Downhole Array (GVDA: Chandra *et al.*, 2015), and use the model from Archuleta *et al.* (1992).

## 2. Wave propagation model

We consider the following model for vertically propagating shear waves in a downhole array where soil behaviour is approximated as a Kelvin-Voigt solid (Park and Hashash, 2004):

$$\begin{cases} \rho(z)\ddot{u}(z,t) = (G(z,t)u_z(z,t) + \eta(z,t)\dot{u}_z(z,t))_z, & (z,t) \in ]0,L[\times]0,T], \\ u(z,0) = \dot{u}(z,0) = 0, & z \in [0,L], \\ u_z(0,t) = 0, \quad u(L,t) = d_1(t), & t \in [0,T]. \end{cases} \quad (1)$$

Herein, sub-indices $z$ denote spatial derivatives, whereas dot notation is employed for temporal derivatives. Coefficients $\rho$, $G$, and $\eta$ represent density, shear modulus, and viscosity, respectively, whereas $u(z, t)$ denotes horizontal displacement. Function $d_1(t)$ is the recorded downhole horizontal displacement at depth $L$, and $[0,T]$ is the data recording interval.

In the linear model $\tau = G\gamma + \eta\dot{\gamma}$, where $\gamma = u_z$ denotes strain, energy dissipation from loading/unloading cycles is approximated by the viscosity term, but such an estimate is not valid for strong motion. In this work, we render the model more sensitive to large strains by letting linear parameters $G$ and $\eta$ depend on pore-water pressure. For this purpose, we consider the shear modulus degradation introduced by Matasovic and Vucetic (1993):

$$G(z,t) = G_0(z)\sqrt{1 - P^\star}, \quad (2)$$

where $G_0$ is the initial shear modulus and $P^*$ is the excess pore-water pressure ratio. Groholski *et al.* (2014) refer to factor $\sqrt{1 - P^\star}$ as the shear modulus degradation index, which accounts for the reduction of effective stresses and the corresponding degradation of shear modulus due to excess pore-water pressure generation.

The formula for the viscous damping coefficient is based on a quadratic relationship between shear modulus and damping ratio proposed by Ishibashi and Zhang (1993):

$$\eta(z,t) = D_0(z)\left[0.586\left(\frac{G(z,t)}{G_{max}}\right)^2 - 1.547\left(\frac{G(z,t)}{G_{max}}\right) + 1\right]G(z,t), \quad (3)$$

where $D_0$ represents the maximum damping coefficient. Eq. 3 introduces through shear modulus the dependence of viscosity on $P^*$. Since pore-water pressure is coupled with strain, the model is no longer linear. However, since we restrict ourselves to the situation where $P^* = P^*(z,t)$ is available as input data, Eq. (1) remains linear.

We assume the medium is composed of $N_l$ horizontal layers and coefficients $\rho$, $G_0$, and $D_0$ are homogeneous within each layer, i.e.:

$$\begin{cases} \rho(z) & \approx & \rho_l, \\ G_0(z) & \approx & G_{0,l}, \\ D_0(z) & \approx & D_{0,l} \end{cases} \quad (4)$$

in the $l$-th layer ($1 \leq l \leq N_l$). Because some layers might contain multiple piezometers, a computational grid with $N_e \geq N_l$ cells (elements) is chosen such that: 1) each layer has at most one element;

2) no element is shared by adjacent layers; and 3) each element has at most one pore-water pressure observation point, as illustrated in Fig. 1. This grid will be employed in the spectral-element discretization of Eq. 1. We approximate $G(z,t)$ and $\eta(z,t)$ at the $e$-th element as follows:

$$G(z,t) \approx G_e(t) := G_{0,l}\sqrt{1 - P_e^\star(t)}, \tag{5}$$

$$\eta(z,t) \approx D_{0,l}\left[0.586\left(\frac{G_e(t)}{G_{max}}\right)^2 - 1.547\left(\frac{G_e(t)}{G_{max}}\right) + 1\right]G_e(t), \tag{6}$$

where $l$ identifies the layer where the element is located, $P_e^*(t) = P^*(\bar{z}_e, t)$ and $\bar{z}_e$ is the observation point of the $e$-th element. On the other hand, the domain discretization cannot handle the fact that some of the $P_e^*$ may not be available. This difficulty will be addressed in the next section.

In summary, the input parameters of the proposed model are the material properties $\{\rho_l, G_{0,l}, D_{0,l}\}$ for $l = 1,...,N_l$ as well as the time histories of excess pore-water pressure ratios $P_e^*(t)$ ($1 \leq e \leq N_e$), and the downhole displacement $d_1(t)$.
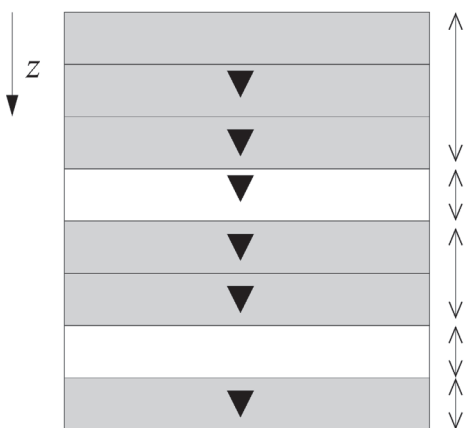


Fig. 1 - A five-layer model ($N_l$ = 5) discretized with a uniform grid with eight elements ($N_e$ = 8). Each element has at most one piezometer (black triangle).

## 3. Parameter selection

Let us proceed to the selection of input parameters to the viscoelastic model of Eq. 1. We regard as input data the following:
- the downhole displacement $d_1(t)$,
- the thickness $H_l$ and the density $\rho_l$ at each layer $l$ ($0 \leq l \leq N_l$),
- the excess pore-water pressure ratio $P^*(z,t)$,

but we assume that the latter is measured only in a few observation points $z_1$, where $P_i(t) = P^*(z_i, t)$.

To infer the excess pore-water pressure ratio $P_e^*(t)$ at an element $e = 7$ that does not contain observation points (such as in Fig. 1), let us first consider the case where the average depth is bounded by two observation points, i.e., $z_i \leq \bar{z}_e \leq z_j$. We employ linear interpolation between $P_i(t)$ and $P_j(t)$:

$$P_e^\star(t) = w_{1,e}P_i(t) + w_{2,e}P_j(t). \tag{7}$$

For example, if the fourth element was centred at $\bar{z}_4 = 10$ m, and the closest observation points around it were $z_2 = 8$ m and $z_3 = 14$ m, then we would select $P_4^*(t) = (2/3)P_2(t) + (1/3)P_3(t)$.

On the other hand, when the $e$-th element is shallower or deeper than all observation points (such as $e = 1$ in Fig. 1), we estimate $P_e^*(t)$ as follows:

$$P_e^\star(t) = P_i(\gamma_e t),\qquad(8)$$

where $i$ is the index of the closest observation point and $\gamma_e$ is a time-scaling factor to account for the fact that the variation of pore-water in one layer can be significantly faster (or slower) than in another (Cubrinovski and Bradley, 2008). The time-scaling factor $\gamma_e$ allows $P_i(\gamma_e t)$ to evolve faster ($\gamma_e \leq 1$) or slower ($0 \leq \gamma_e \leq 1$) than $P_i(t)$.

Material properties $G_{0,l}$ and $D_{0,l}$, as well as scaling factors $\gamma_e$ are determined by solving an inverse problem. For this purpose, we define the parameter vector:

$$\boldsymbol{m} = [G_{0,1}, \ldots, G_{0,N_l}, D_{0,1}, \ldots, D_{0,N_l}, \gamma_1, \ldots, \gamma_Q],\qquad(9)$$

where $Q \leq N_e$ is the number of elements where excess pore-water pressure ratio is estimated as in Eq. 8. Thus, we have a total of $N = 2N_l + Q$ unknown parameters. We remark that a more general scheme would regard $H_l$ and $\rho_l$ as parameter models as well.

Let $\boldsymbol{u}_n(\boldsymbol{m}), \boldsymbol{v}_n(\boldsymbol{m})$, and $\boldsymbol{a}_n(\boldsymbol{m}), 0 \leq n \leq N_t$, be the surface ground motion components using input data $\boldsymbol{m}$ at the time samples $t_0,\ldots,t_{Nt}$. The first entries of these vectors, $\{u_{1,n}(\boldsymbol{m}), v_{1,n}(\boldsymbol{m}), a_{1,n}(\boldsymbol{m})\}$, approximate the observed surface displacement, velocity, and acceleration, $\{d_0(t_n), v_0(t_n), a_0(t_n)\}$.

We seek $\boldsymbol{m} = 3(N_t + 1)$ the parameter vector $\boldsymbol{m}$ that minimizes the relative misfit between predicted data

$$\boldsymbol{d}(\boldsymbol{m}) = [u_{1,0}(\boldsymbol{m}), \ldots, u_{1,N_t}(\boldsymbol{m}), v_{1,0}(\boldsymbol{m}), \ldots, v_{1,N_t}(\boldsymbol{m}), a_{1,0}(\boldsymbol{m}), \ldots, a_{1,N_t}(\boldsymbol{m})],\qquad(10)$$

which has a total of $M = 3(N_t + 1)$ components, and the observed data

$$\boldsymbol{d}^{obs} = [d_0(t_0), \ldots, d_0(t_{N_t}), v_0(t_0), \ldots, v_0(t_{N_t}), a_0(t_0), \ldots, a_0(t_{N_t})],\qquad(11)$$

i.e. we seek the solution to the nonlinear least squares problem $\min\{E(\boldsymbol{m}) ; \boldsymbol{m} \in I\!\!R^N\}$ where the misfit function satisfies

$$E^2(\boldsymbol{m}) = \frac{\sum_{n=0}^{N_t}(d_0(t_n) - u_{1,n}(\boldsymbol{m}))^2}{\sum_{n=0}^{N_t} d_0^2(t_n)} + \frac{\sum_{n=0}^{N_t}(v_0(t_n) - v_{1,n}(\boldsymbol{m}))^2}{\sum_{n=0}^{N_t} v_0^2(t_n)} + \frac{\sum_{n=0}^{N_t}(a_0(t_n) - a_{1,n}(\boldsymbol{m}))^2}{\sum_{n=0}^{N_t} a_0^2(t_n)}.\qquad(12)$$

The minimization of the misfit function (Eq. 12) is carried out with a global optimization algorithm, namely the Very Fast Simulated Annealing (VFSA), and the resulting model is subsequently refined with a WGN local optimization technique (Fig. 2). Both algorithms depend on successive evaluations of the misfit function $E(\boldsymbol{m})$. In order to compute the predicted data $\boldsymbol{d}(\boldsymbol{m})$, needed in $E(\boldsymbol{m})$, we use the spectral element method (SEM). In Appendix A we provide details on SEM and both inversion algorithms.
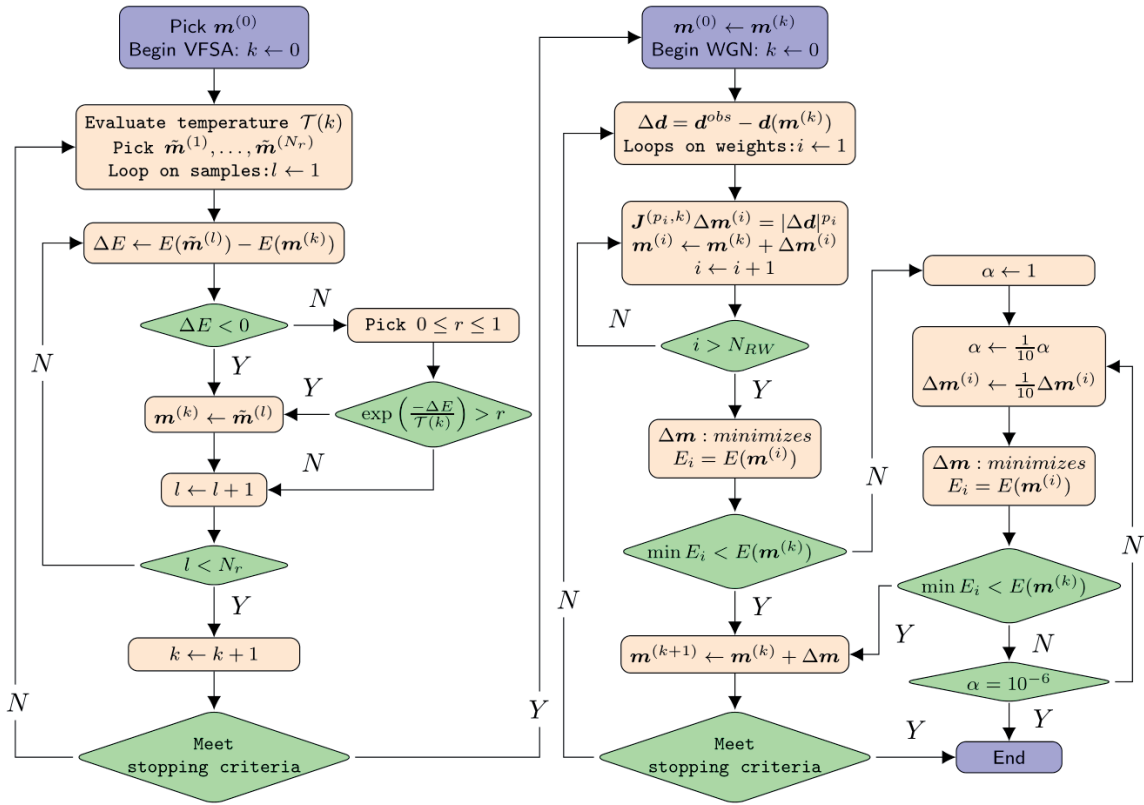
Fig. 1 - Flowchart of the inversion algorithm.

## 4. Examples

In the following we apply the inversion algorithm presented in the previous section to the Superstition Hills and the Southern California earthquakes. In order to highlight how pore-water pressure information improves the model, we compare our methodology with the inverse process based on the following time-invariant expression for shear modulus:

$$G(z,t) = G_0(z). \tag{13}$$

In this case, the parameter vector becomes

$$\boldsymbol{m} = [G_{0,1}, \ldots, G_{0,N_l}, D_{0,1}, \ldots, D_{0,N_l}]. \tag{14}$$

From here on, we refer to Eqs. 13 and 2 as the *plain linear* and the *transient linear* models, respectively.

The spatial discretization is done with spectral elements of degree $N_p = 4$, and the time discretization step is $\Delta t = 0.005$ s, so that the predicted data $\boldsymbol{d}(\boldsymbol{m})$ will have 200 samples per second. By an approximate numerical dispersion analysis (Appendix B), we have verified that the numerical solution is accurate for frequencies up to 7.7 Hz in WLA and 20.6 Hz in GVDA.

Let us choose the VFSA *a priori* bounds $[m_i^{min}, m_i^{max}]$ from Appendix A. The bounds for stiffness modulus are $G_{o,l} \in [0.9G_{o,l}^r, 1.1G_{o,l}^r]$ ($l = 1,\ldots,N_l$), where $G_{o,l}^r$ are reference values from the literature, specified in Sections 4.1 and 4.2. From the damping factors reported by Ishibashi and Zhang (1993) for a variety of soils, the interval from 0 to 50% should account for expected values of the damping coefficient, noting that commonly accepted values for the damping ratio are used for the damping coefficient (Ching and Glaser, 2001). Thus, we impose $D_{o,l} \in [0, 0.5]$ ($1 \leq l \leq N_l$). Time-scaling factors $\gamma_l$ should be selected observing that the liquefaction process propagates sequentially downwards (Holzer and Youd, 2007). Thus, we expect faster variation of pore pressure in the shallower layers ($\gamma_l \in [1,5]$) and slower variation in the deeper ones ($\gamma_l \in [1/5, 1]$), and we impose $\gamma_l \leq \gamma_{l-1}$ for $2 \leq l \leq Q$.

The experiments have been implemented in the programming language Fortran 90 and have been carried out in a notebook with 16 Gb RAM and a 2.40 GHz Intel© Core i7-4700HQ processor.

### 4.1. 1987 Superstition Hills earthquake

Our first example is the 1987 Superstition Hills earthquake, using data from the Imperial Valley Wildlife Liquefaction Array (WLA). We refer to Bennett *et al.* (1984), Brady *et al.* (1989), and Youd and Holzer (1994) for a comprehensive description of the site, instrumentation, and recordings. In this work we employ data reported in Brady *et al.* (1989), which is available from ftp://ftp.ngdc.noaa.gov/hazards/cdroms/EQ_StrongMotion_v1/data/usaca41/.

This data set provides displacements, velocities, and accelerations with 200 samples per second, and pore-water pressures with 50 samples per second.

We select $T = 96.98$ s, $L = 7.5$ m, and take $d_1(t)$ as the 360-degree (N-S) component direction of the displacement vector recorded at 7.5 m depth. This channel is the most frequently studied in the literature. Moreover, the N-S component had the highest peak ground acceleration (*PGA*). Regarding the material properties, we consider the model with $N_l = 4$ layers from Bonilla *et al.* (2005), depicted in Fig. 3. The number of elements of the mesh is given by $N_e = 9$.
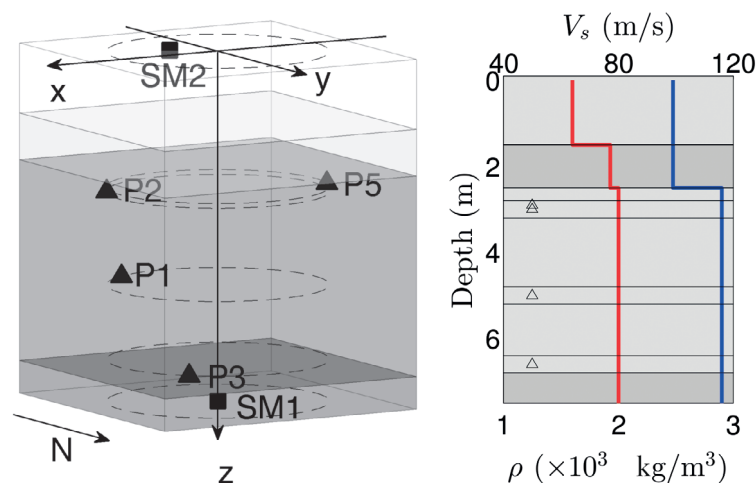


Fig. 3 - Left: sketch of the WLA layered model. The seismometers (SM1 and SM2) and the piezometers (P1 to P3, P5) are located according to Bennett *et al.* (1984). Right: profiles of shear velocity (blue) and density (red); horizontal lines denote grid cells.

We consider the recordings from piezometers P1, P2, P3, and P5, which are located at depths 5.0, 3.0, 6.6, and 2.9 m, respectively. Following Holzer and Youd (2007), the excess pore-water pressure ratio is found by first taking the excess pore-water pressure relative to static pore-water pressure at the beginning of the earthquake and dividing it by the recorded value at 96.98 s.

Note that piezometers P2 and P5 are nearly at the same depth, namely the centre $\bar{z}_4 = 3$ m of the fourth layer. Since piezometer P5 is regarded as the most reliable (Holzer and Youd, 2007), we discard piezometer P2. The pore-water pressure ratios at each layer are chosen according to the guidelines of Section 3, with $Q = 3$ unknown time-scale factors:

$$P_1^\star(t) = P_5(\gamma_1 t), \quad P_2^\star(t) = P_5(\gamma_2 t), \quad P_9^\star(t) = P_3(\gamma_3 t). \tag{15}$$

Ching and Glaser (2001) noted that the plain linear model (Eq. 13) is not able to predict the surface displacements observed in WLA. This can be clearly noted from the calculated displacement (Fig. 4), which is nearly the same as in Fig. 10 in Ching and Glaser (2001). As pointed out therein, by using constant $G$ and $\eta$ one cannot account for the soil weakening that starts from the pore-water pressure buildup at approximately 13 s. On the other hand, a substantial improvement, in both amplitude and phase, is observed with the transient linear model.
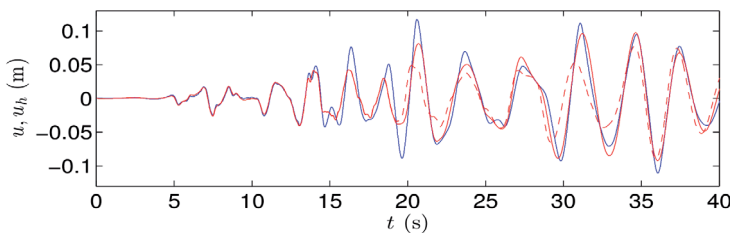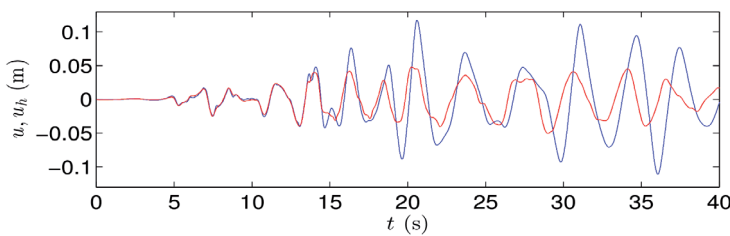


Fig. 4 - WLA N-S surface displacement of recorded data (blue), numerical approximation (red) and initial guess (red, dashed) obtained with the plain (top) and transient (bottom) linear models.
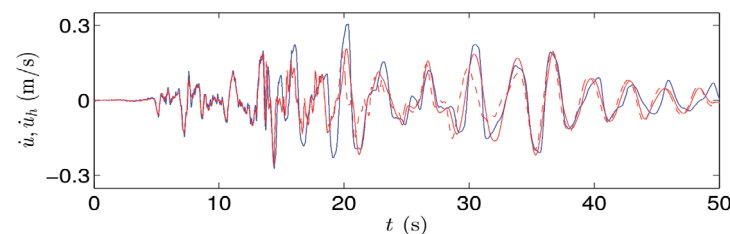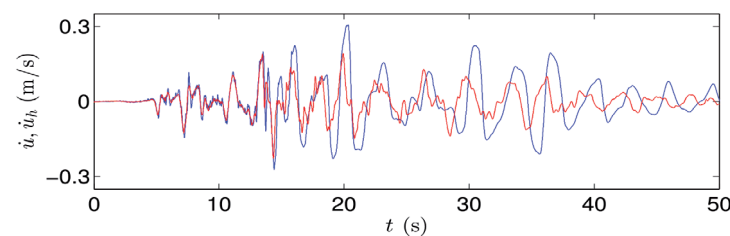
Fig. 5 - WLA N-S surface velocity of recorded data (blue), numerical approximation (red) and initial guess (red, dashed) obtained with the plain (top) and transient (bottom) linear models.
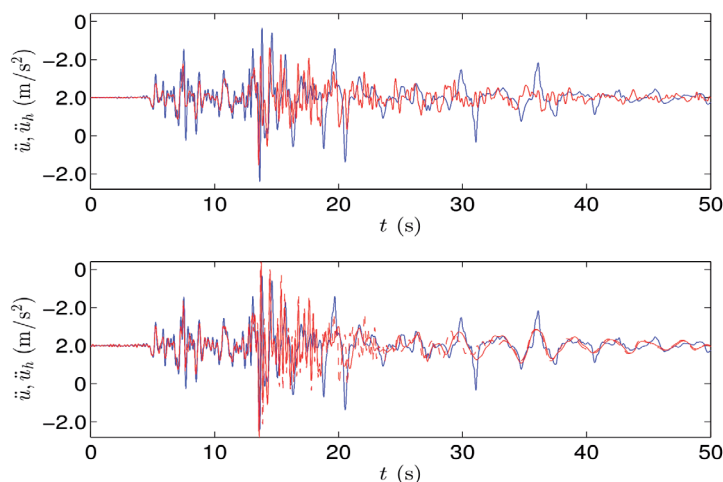
Fig. 6 - WLA N-S surface acceleration of recorded data (blue), numerical approximation (red) and initial guess (red, dashed) obtained with the plain (top) and transient (bottom) linear models.

Surface velocities and accelerations of the plain and transient linear models are compared in Figs. 5 and 6 respectively, under the same settings as in Oral *et al.* (2017). Again, approximations of surface velocity and acceleration by the transient linear model have been more accurate than the plain linear model. By comparing the results of the transient linear model with Figs. 8 and 9 of Oral *et al.* (2017), one can note that the velocities are concordant. Our estimate is less accurate near $t = 15$ s, but the low-frequency content is better represented starting from $t = 20$ s. Fig. 7 shows the excess pore-water pressure ratios recorded and computed at each layer. The pore-water pressure build up is more significant at the first two layers (0 - 2.5 m).
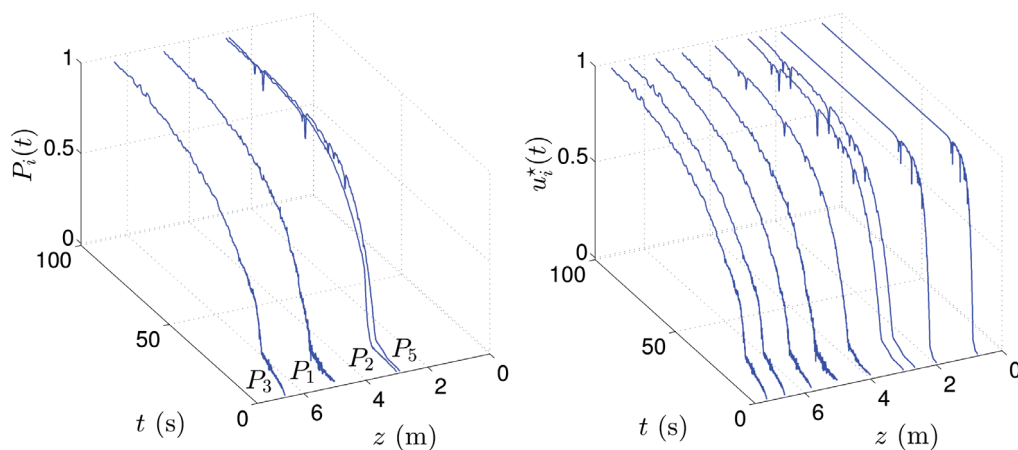


Fig. 7 - WLA excess pore-water pressure ratios: recorded data from piezometers P1 to P5 (left) and estimates obtained from the transient linear model (right).

Fig. 8 displays the response spectrum, as in Figs. 11, 12 and 14 of Groholski *et al.* (2014). The spectral response of the plain linear model is closer to the response of recorded data for short periods, but in general the spectral response is underestimated. The transient linear model provides better responses for most periods, especially the longer ones. Moreover, the results of the transient linear model are much closer to the best fitted model (SelfSim - Pass 13) obtained in

Groholski *et al*. (2014) than the ones form the initial model employed therein. Hence, the transient linear model could provide useful initial models for nonlinear site-response analysis.
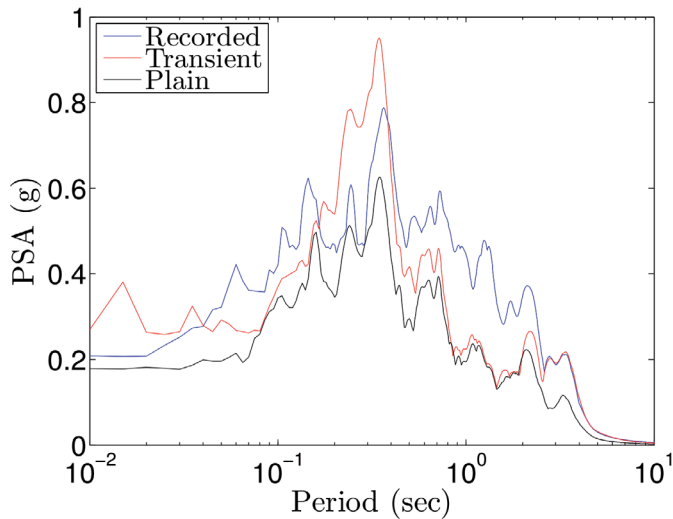


Fig. 8 - WLA response-spectrum obtained from recorded data (blue), along with the plain (black) and transient (red) linear models.

Figs. 9 and 10 display the stress-strain histories of the transient and plain linear models, respectively. The red colour denotes the interval [10, 15], where liquefaction took place. Note that the stress-strain history of the transient linear model is more sensitive to large strains than the plain linear model. In particular, the strains predicted by the transient linear model at 3 m are more consistent with the average approximation proposed by Zeghal and Elgamal (1994) and the predictions by Oral *et al.* (2017) (Fig. 11).
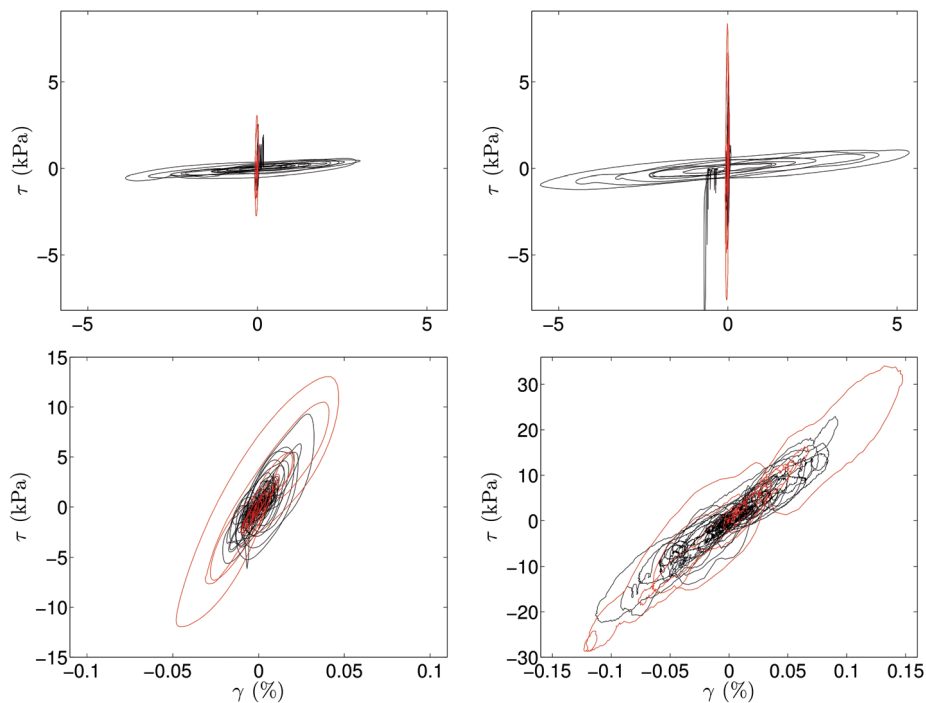


Fig. 9 - Stress-strain history of the transient linear model at depths $z = 0.75$ (a), $z = 2$ (b), $z = 3$ (c), and $z = 7.15$ (d) corresponding to time interval [0, 50] (in seconds). The time interval [10, 15] is marked in red.
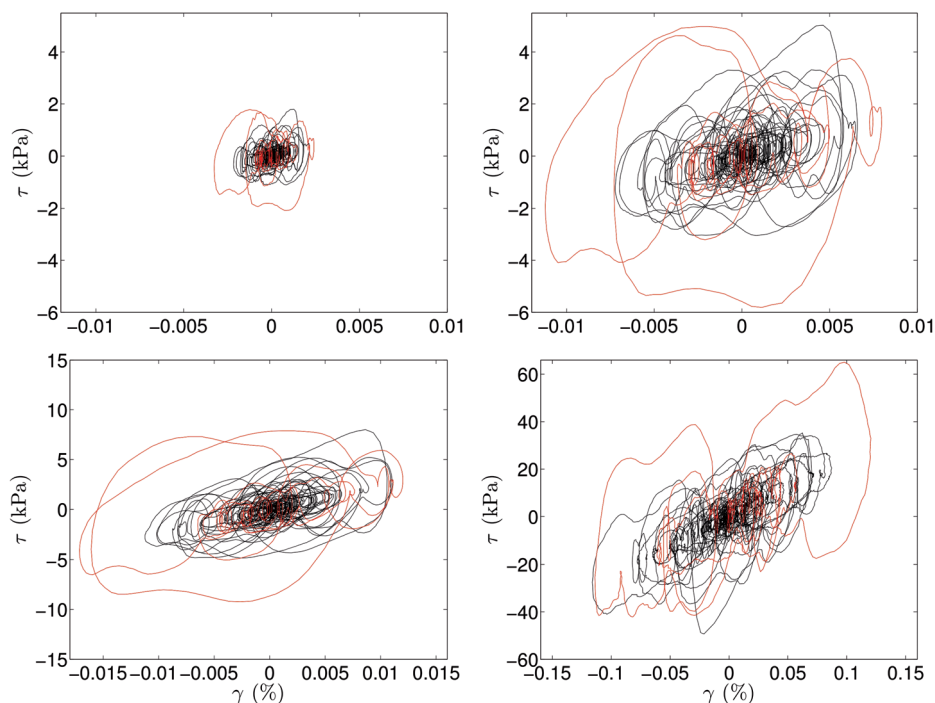
Fig. 10 - Stress-strain history of the plain linear model at depths $z = 0.75$ (a), $z = 2$ (b), $z = 3$ (c), and $z = 7.15$ (d) corresponding to time interval [0, 50] (in seconds). The time interval [10, 15] is marked in red.

Let us proceed to the details of the inversion process. In the transient model, the misfit has reduced from 1.5344 to 1.2057 with VFSA algorithm, and from 1.2057 to 1.2053 with two iterations of WGN. In the plain linear model, the misfit reduction was from 1.6824 to 1.6819 in VFSA and from 1.6819 to 1.6818 with WGN (three iterations). The CPU time spent on VFSA and Gauss-Newton methods was respectively 35506 s and 74 s in the plain linear model, and 36890 s and 66 s in the transient linear model.

It is worth noting that the transient linear model has reached better fitness with only three additional entries in the parameter vector. In other words, the inversion algorithms have been more sensitive to these parameters than the other 8. The parameters of the inverted model considering both plain linear and transient linear models are presented in Table 1. For an easier comparison, the damping coefficients of the transient linear are presented at minimal (when $G/G_{max} = 1$) rather than maximal values. In general, the transient linear model predicts lower soil stiffness than the reference model (Bonilla *et al.*, 2005). Moreover, the minimal viscous damping coefficients were roughly 0.02, similarly to the values employed by Ching and Glaser (2001). In the plain linear model, the algorithm has led to (constant) damping coefficients that are much higher than those proposed by Ching and Glaser (2001).

The last two experiments in this example verify the consistency of the inversion process and the proposed model by using the inverted parameters to predict other surface motions. Let us begin with data from the same event, namely the 90-degree (E-W) component direction of the ground motion (Figs. 11 to 13). The misfit of the plain and transient linear models were 1.3224 and 1.7487, respectively. Again, the assimilation of pore-water pressure data has improved the approximation with respect to the plain linear model.

Table 1 – Estimated parameters of the plain and transient linear models for the 1987 Superstition Hills earthquake.

| | Plain linear | | Transient Linear | | |
|---|---|---|---|---|---|
| $l$ | $G_{0,l}$ (KPa) | $D_{0,l}$ (s) | $G_{0,l}$ (KPa) | $D_{min,l}$ (s) | $\gamma_l^r$ |
| 1 | 14924.7947 | 0.5000 | 14113.4400 | 0.0098 | 4.9990 |
| 2 | 17313.6739 | 0.3000 | 17006.6952 | 0.0127 | 3.4915 |
| 3 | 24220.8000 | 0.1633 | 24248.2789 | 0.0195 | 1.0000 |
| 4 | 24230.1470 | 0.2360 | 24220.8000 | 0.0195 | — |
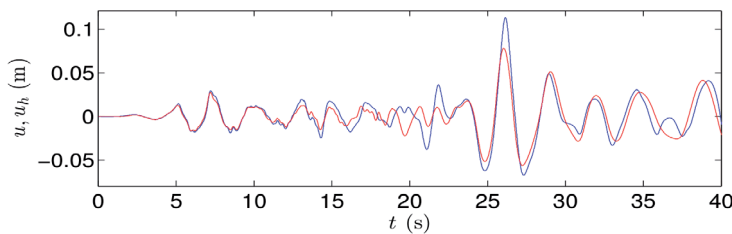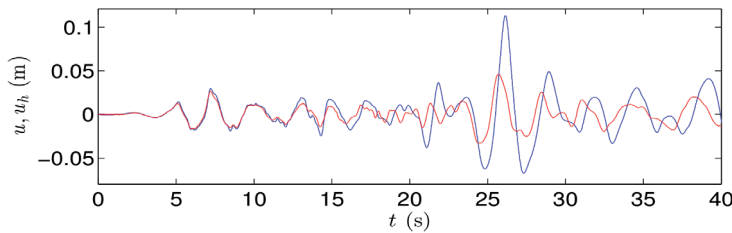


Fig. 11 - WLA E-W surface displacement of recorded data (blue), numerical approximation (red) obtained with the plain (top) and transient (bottom) linear models.
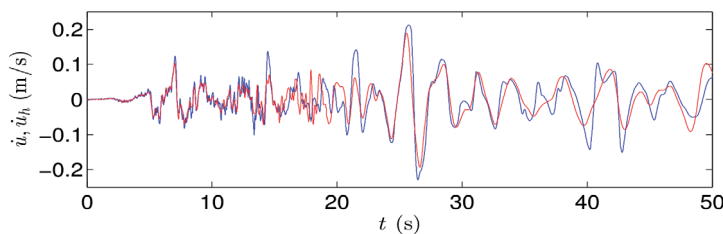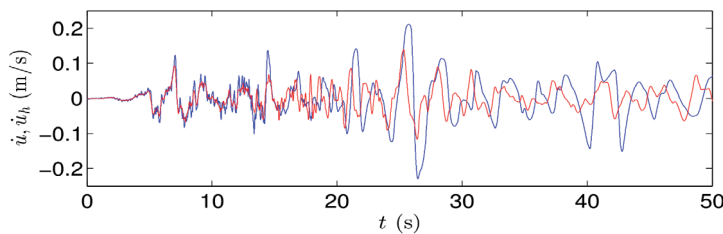


Fig. 12 - WLA E-W surface velocity of recorded data (blue), numerical approximation (red) obtained with the plain (top) and transient (bottom) linear models.

Let us now consider a different data set, the *M* 5.4 Brawley earthquake of 26 August 2012, 20:57 UTC (Hauksson *et al.*, 2013). The data set is available in the database maintained by the Network for Earthquake Engineering Simulation (NEES) at the University of California at Santa Barbara (http://nees.ucsb.edu/data-portal).
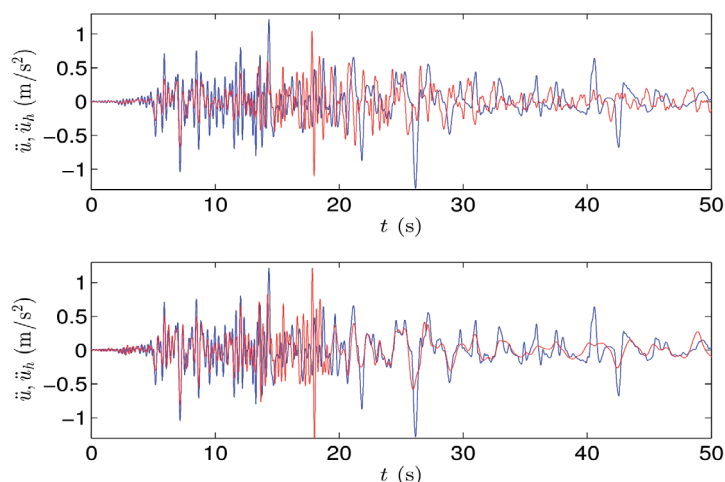
Fig. 13 - WLA E-W surface acceleration of recorded data (blue), numerical approximation (red) obtained with the plain (top) and transient (bottom) linear models.

The instruments in the original WLA site have been replaced, and we have used the data from a downhole seismometer at 7.7 m, and three piezometers at 3.0, 4.4, and 5.8 m. A new grid has been set in order that the piezometers be located at the middle of the elements, and internal elements without piezometers be nearly equally spaced between two of them.

Figs. 14 to 16 show the N-S surface displacements, velocities, and accelerations predicted by the plain and transient linear models. Even though the transient linear model provided a lower misfit (1.2266) from observed surface data than plain linear (1.3751), there is no apparent improvement in the figures, unlike observed in the data from Superstition Hills.

### 4.2. 2010 Southern California earthquake

The $M$ 5.4 Southern California earthquake of 7 July 2010 took place on the San Jacinto Fault, and was triggered by the 2010 $M$ 7.2 El Mayor-Cucapah earthquake sequence (Hauksson *et al.*,
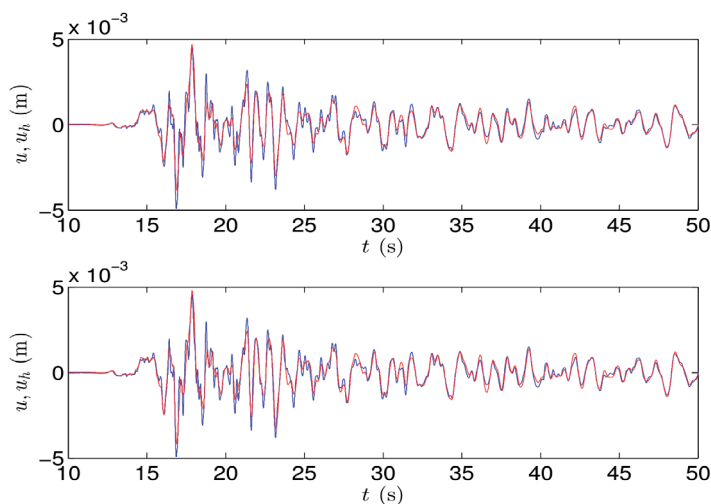


Fig. 14 - $M$ 5.4 Brawley earthquake N-S surface displacement of recorded data (blue), numerical approximation (red) obtained with the plain (top) and transient (bottom) linear models.
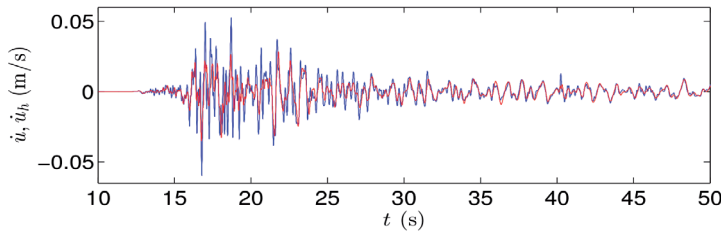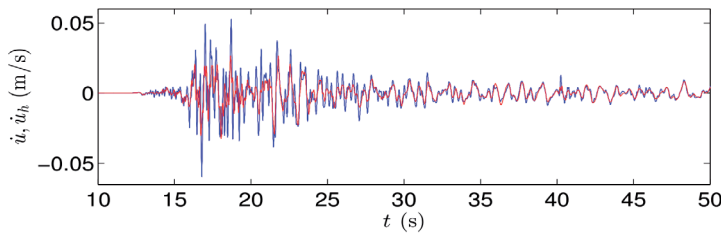
Fig. 15 - *M* 5.4 Brawley earthquake N-S surface velocity of recorded data (blue), numerical approximation (red) obtained with the plain (top) and transient (bottom) linear models.
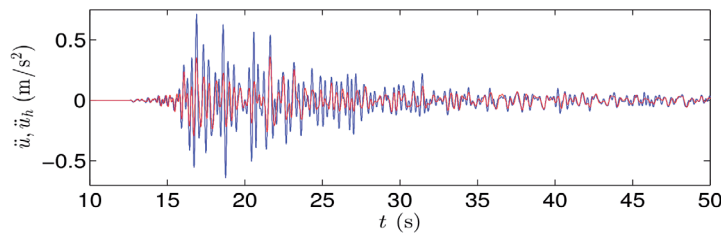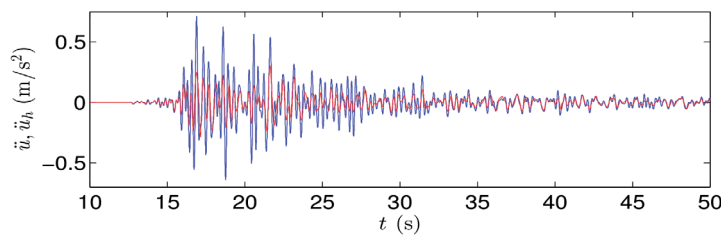


Fig. 16 - *M* 5.4 Brawley earthquake N-S surface acceleration of recorded data (blue), numerical approximation (red) obtained with the plain (top) and transient (bottom) linear models.

2011). We use the recordings from the GVDA, which are also available in the database maintained by NEES.

Among the several stations available for this event, we have selected the accelerometers located at 0 and 15 m (so $L = 15$ m) and the E-W components of the recorded data, which had the highest $PGA$. We compute the velocities and displacements following the procedure from Converse and Brady (1992). The sampling interval is 0.005 s, and we study the first 100 s of the recordings, i.e. 100 s. We consider the first seven layers of the model from Archuleta *et al.* (1992), outlined in Fig. 17, so that $N_l = 7$, and select the piezometers located at depths 3.5, 6.2, 8.8, 10.1, and 12.4 m, which we refer to as P1, P2, P3, P4 and P5. As in WLA, the number of elements is $N_e = 9$.

We select $P_i^*(t)$ analogously to the previous example (now $Q = 2$):
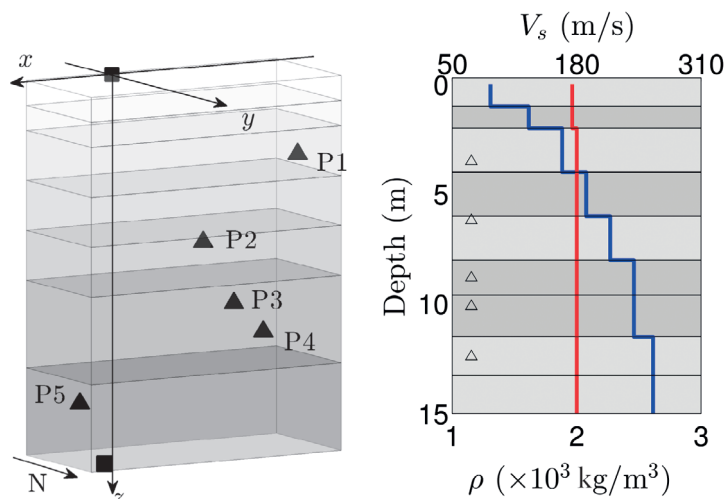
Fig. 17 - Left: sketch of the GVDA layered model. The seismometers and piezometers are located according to NEES data. Right: profiles of shear velocity (blue) and density (red); horizontal lines denote grid cells.

$$\begin{cases} P_i^\star(t) &= P_1(\gamma_i t) \quad (1 \leq i \leq 2), \\ P_3^\star(t) &= P_1(t) \\ P_4^\star(t) &= 0.4444 P_1(t) + 0.5556 P_2(t), \\ P_5^\star(t) &= 0.6923 P_2(t) + 0.3077 P_3(t), \\ P_i^\star(t) &= P_{i-3}(t) \quad (6 \leq i \leq 8), \\ P_9^\star(t) &= P_5(t). \end{cases} \quad (16)$$

Fig. 18 compares surface velocities and accelerations from recorded data with those estimated from the transient linear model and from observed data. The plain linear model is slightly less accurate (in the sense that it presents a higher misfit, as reported below) but provides similar plots of the three surface components, and for this reason, its figures are not shown here. Similarly to same case studies reported by Ching and Glaser (2001), the plain linear model has been sufficient to predict surface motion. Fig. 19 shows the calculated excess pore-water pressure ratios along with the recorded excess pore-water pressure ratios. As in Fig. 7, the inversion algorithm has led to a faster development of pore-water pressure in the shallower layers.
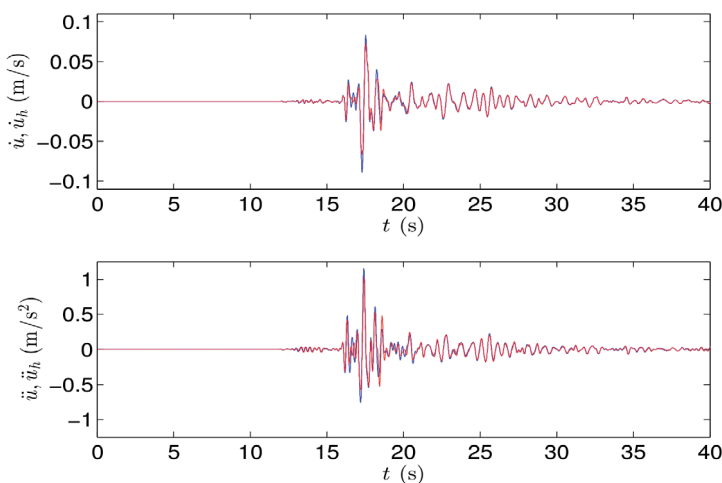


Fig. 18 - GVDA surface velocity (top) and acceleration (bottom) of recorded data (blue) and the numerical approximation obtained with the transient linear model (red).
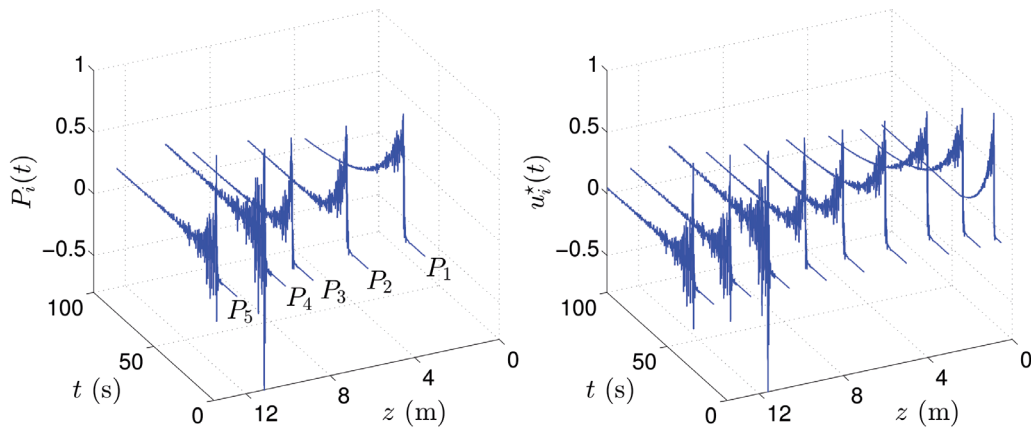
Fig. 19 - GVDA excess pore-water pressure ratios: recorded data from piezometers P1 to P5 (left) and estimates obtained from the transient linear model (right).

Fig. 20 shows response spectrum, as in Fig. 8. As in WLA, the plain linear model is more accurate for short periods but underestimates the response for longer periods.
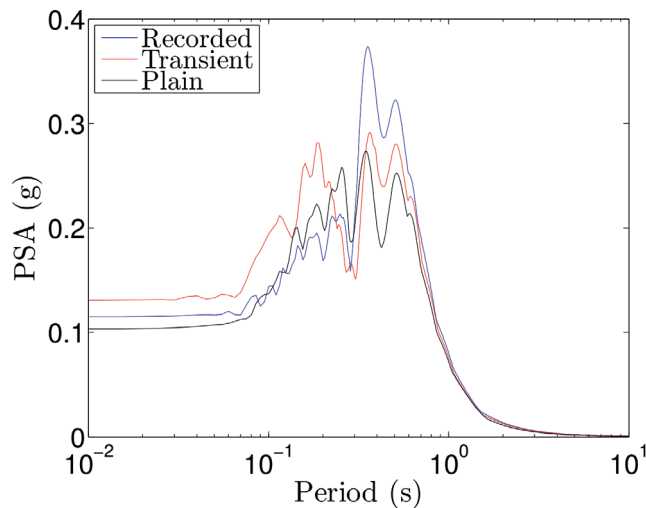


Fig. 20 - GVDA response-spectrum obtained from recorded data (blue), along with the plain (black) and transient (red) linear models.

Regarding misfit values, in the transient model, we have observed a reduction from 0.6286 to 0.4980 with VFSA algorithm, and from 0.4980 to 0.4944 with eight iterations of WGN. In the plain linear model, the misfit reduction was from 0.8602 to 0.5858 in VFSA and from 0.5858 to 0.5559 with WGN (five iterations). During execution of this experiment with the plain linear model, the CPU times in the VFSA and Gauss-Newton were 33329 and 181 s, respectively. For the transient linear model, these times were 37412 and 360 s, respectively.

We conclude this section with Table 2 showing the inverted parameters of the plain linear and transient linear models. As in WLA, the transient linear model predicts lower soil stiffness than the reference model (Archuleta *et al.,* 1992), but the viscous damping coefficients at maximum

shear modulus, which range from 0 to 0.02, are lower than the ratio $\eta/G$ employed by Ching and Glaser (2001). The inverted parameters of the plain linear model are generally concordant with the transient one, except for a high constant damping in the first layer.

## 5. Discussion and conclusions

We have studied a linear, 1D viscoelastic model that incorporates pore-water pressure measurements as input data. This approach is intermediate between plain linear models, which do not properly account for liquefaction, and nonlinear models, whose parameters are less straightforward (Kwok *et al.,* 2007). The interpolated pore-water pressure obtained through inversion may be useful in nonlinear studies of pore-water pressure prediction, for instance as an initial guess for an iterative nonlinear solver. Moreover, as noted in Hashash and Park (2001), initial estimates of modulus and damping are needed in an iterative scheme for a nonlinear soil model.

Our numerical results show that the pore pressure was the crucial component to understand the displacement registered in the surface, besides bringing satisfactory results in the inversion process. Taking into account the data presented at the 1987 Superstition Hills earthquake event, liquefaction was one of the factors that resulted in an increase of surface motion amplitude after 13.6 s. In this respect, Ching and Glaser (2001) have observed that the parameters $G,\eta$ cannot remain constant under liquefaction, justifying the introduction of a model dependent on shear-deformation and pore-pressure as defined by Eqs. 2 and 3. Despite the non-linearity of these parameters, the model can be considered linear since the pore pressures were not updated iteratively from the motion data.

The linearity of the model presented in this text may explain the slight superiority of the model proposed by Oral *et al.* (2017) in relation to ours, since our methodology may overestimate the material strength under strong input motion. We also recognize that relationships defined by Eqs. 2 and 3 do not describe a hysteretic behaviour differently from material implemented by Oral *et al.* (2017), which is modelled through a combination of viscoelasticity and hysteretic behaviour. This limitation has produced results with large misfit. However, we believe that non-linear models incorporated into our methodology and including hysteresis may decrease the error significantly.

Table 2 - Estimated parameters of the plain and transient linear models for the Southern California earthquake.

| | Plain linear | | Transient linear | | |
|---|---|---|---|---|---|
| $l$ | $G_{0,l}$ (KPa) | $D_{0,l}$ (s) | $G_{0,l}$ (KPa) | $D_{min,l}$ (s) | $\gamma_l^r$ |
| 1 | 17374.5000 | 0.5000 | 16980.7022 | 0.0195 | 2.8247 |
| 2 | 36250.5000 | 0.0224 | 32632.8054 | 0.0049 | 1.2062 |
| 3 | 49005.0000 | 0.0254 | 53511.9271 | 0.0195 | — |
| 4 | 65301.2916 | 0.0140 | 65955.1638 | 0.0104 | — |
| 5 | 86674.6698 | 0.0132 | 84368.6423 | 0.0104 | — |
| 6 | 103680.0000 | 0.0155 | 110490.6352 | 0.0003 | — |
| 7 | 121680.0000 | 0.0142 | 121761.3777 | 0.0003 | — |

By comparing the inversion results with and without pore-water pressure ratios, we conclude that these parameters are an essential ingredient for a model to account for strong ground motion. This finding, which has been reported in the literature for nonlinear models, can thus be extended to the linear model. Further support for the validity of the proposed transient linear model arises from the comment by Groholski *et al.* (2014) that soil behaviour tends to become more linear over a wider range of shear strains as excess pore pressures increase.

Besides the natural limitation of not accounting for nonlinear effects, the transient linear may not sufficiently account for damping mechanism. The method should benefit from a full Rayleigh damping formulation (Kwok *et al.*, 2007). For the Superstition Hills earthquake, one could explore the radial symmetry of the piezometers' locations (Fig. 3) by considering an axisymmetric viscoelastic model. In this model, one could explicitly consider surface waves, which are an important element of long-period strong motions (Holzer and Youd, 2007). The inversion could also increase the number of layers, providing higher-resolution models for the study areas.

REFERENCES

Archuleta R.J., Seale S.H., Sangas P.V., Baker L.M. and Swain S.T.; 1992: *Garner Valley downhole array of accelerometers: instrumentation and preliminary data analysis*. Bull. Seismol. Soc. Am., **82**, 1592-1621.

Bennett M.J., McLaughlin P., Sarmiento J. and Youd T.; 1984: *Geotechnical investigation of liquefaction sites, Imperial Valley, California*. U.S. Geological Survey, Menlo Park, CA, USA, Open-File Report 84-252, 108 pp.

Björck A.; 1996: *Numerical methods for least squares problems*. SIAM, Philadelphia, PA, USA, 408 pp.

Bonilla L.F., Archuleta R.J. and Lavallée D.; 2005: *Hysteretic and dilatant behavior of cohesionless soils and their effects on nonlinear site response: field data observations and modeling*. Bull. Seismol. Soc. Am., **95**, 2373-2395, doi:10.1785/0120040128.

Brady A.G., Mork P.N., Seekins L.C. and Switzer J.C.; 1989: *Processed strong-motion records from the Imperial Wildlife liquefaction array, Imperial County, California, recorded during the Superstition Hills earthquakes, November 24, 1987*. U.S. Geological Survey, Menlo Park, CA, USA, Open-File Report 89-87, 115 pp.

Chandra J., Guéguen P., Steidl J.H. and Bonilla L.F.; 2015: *In situ assessment of the G- curve for characterizing the nonlinear response of soil: application to the Garner Valley downhole*. Bull. Seismol. Soc. Am., **105**, 993-1010, doi:10.1785/0120140209.

Ching J.Y. and Glaser S.D.; 2001: *1D time-domain solution for seismic ground motion prediction*. J. Geotech. Geoenviron., **127**, 36-47, doi:10.1061/(ASCE)1090-0241(2001)127:1(36).

Chopra A.K.; 1995: *Dynamics of structures: theory and applications to earthquake engineering*. Prentice-Hall, Englewood Cliffs, NJ, USA, 789 pp.

Converse A.M. and Brady A.; 1992: *BAP: basic strong-motion accelerogram processing software; version 1.0*. U.S. Geological Survey, Menlo Park, CA, USA, Open-File Report 92-26-A, 174 pp.

Cubrinovski M. and Bradley B.; 2008: *Assessment of seismic performance of soil-structure systems*. In: *Proc.* 18th NZGS Geotechnical Symposium on Soil-Structure Interaction, Auckland, New Zealand, 17 pp.

Du C. and Wang G.; 2015: *Seismic response analysis of heterogeneous soils using 2D spectral element method*. In: Proc. 28th KKHTCNN Symposium on Civil Engineering, Bangkok, Thailand.

Faccioli E., Maggio F., Paolucci R. and Quarteroni A.; 1997: *2D and 3D elastic wave propagation by a pseudo-spectral domain decomposition method*. J. Seismol., **1**, 237-251, doi:10.1023/A:1009758820546.

Fayun L., Haibing C. and Maosong H.; 2017: *Accuracy of three-dimensional seismic ground response analysis in time domain using nonlinear numerical simulations*. Earthquake. Eng. and Eng. Vibr., **16**, 487-498, doi: 10.1007/s11803-017-0401-1.

Groholski D.R., Hashash Y. and Matasovic N.; 2014: *Learning of pore pressure response and dynamic soil behavior from downhole array measurements*. Soil Dyn. Earthquake Eng., **61**, 40-56, doi:10.1016/j.soildyn.2014.01.018.

Hardin B.O. and Drnevich V.P.; 1972: *Shear modulus and damping in soils: design equations and curves*. J. Soil Mech. Found. Div., ASCE, **98**, 667-692.

Hashash Y.M.A. and Park D.; 2001: *Non-linear one-dimensional seismic ground motion propagation in the Mississippi embayment*. Eng. Geol., **62**, 185-206, doi:10.1016/S0013-7952(01)00061-8.

Hauksson E., Stock J., Hutton K., Yang W., Vidal-Villegas J.A. and Kanamori H.; 2011: *The 2010 Mw 7.2 El Mayor-Cucapah earthquake sequence, Baja California, Mexico and Southernmost California, USA: active seismotectonics along the Mexican Pacific Margin*. Pure Appl. Geophys., **168**, 1255-1277, doi: 10.1007/s00024-010-0209-7.

Hauksson E., Stock J., Bilham R., Boese M., Chen X., Fielding E.J., Galetzka J., Hudnut K.W., Hutton K., Jones L.M., Kanamori H., Shearer P.M., Steidl J., Treiman J., Wei S. and Yang W.; 2013: *Report on the August 2012 Brawley earthquake swarm in Imperial Valley, southern California*. Seismol. Res. Lett., **84**, 177-189, doi:10.1785/0220120169.

Holzer T.L. and Youd T.L.; 2007: *Liquefaction, ground oscillation, and soil deformation at the Wildlife array, California*. Bull. Seismol. Soc. Am., **97**, 961-976, doi:10.1785/0120060156.

Hughes T.; 1987: *The finite element method. Linear static and dynamic finite element analysis*. Prentice- Hall, Englewood Cliffs, NJ, USA, 704 pp.

Ingber L.; 1989: *Very fast simulated re-annealing*. Math. Comput. Modell., **12**, 967-973, doi:10.1016/0895-7177(89)90202-1.

Ishibashi I. and Zhang X.; 1993: *Unified dynamic shear moduli and damping ratios of sand and clay*. Soil Found., **33**, 182-191, doi:10.3208/sandf1972.33.182.

Kaklamanos J., Baise L.G., Thompson E.M. and Dorfmann L.; 2015: *Comparison of 1D linear, equivalent-linear, and nonlinear site response models at six KiK-net validation sites*. Soil Dyn. Earthquake Eng., **69**, 207-219, doi:10.1016/j.soildyn.2014.10.016.

Komatitsch D. and Tromp J.; 2002: *Spectral-element simulations of global seismic wave propagation - I. Validation*. Geophys. J. Int., **149**, 390-412, doi:10.1046/j.1365-246X.2002.01653.x.

Kwok A.O., Stewart J.P., Hashash Y.M., Matasovic N., Pyke R., Wang Z. and Yang Z.; 2007: *Use of exact solutions of wave propagation problems to guide implementation of nonlinear seismic ground response analysis procedures*. J. Geotech. Geoenviron. Eng., **133**, 1385-1398.

Matasovic N. and Vucetic M.; 1993: *Cyclic characterization of liquefiable sands*. J. Geotech. Eng., **119**, 1805-1822, doi:10.1061/(ASCE)0733-9410(1993)119:11(1805).

Mercado V., El-Sekelly W., Zeghal M. and Abdoun T.; 2015: *Identification of soil dynamic properties through an optimization analysis*. Comput. Geotech., **65**, 175-186, doi:10.1016/j.compgeo.2014.11.009.

Montoya-Noguera S. and Lopez-Caballero F.; 2016: *Effect of coupling excess pore pressure and deformation on nonlinear seismic soil response*. Acta Geotech., **11**, 191-207, doi:10.1007/s11440-014-0355-7.

Olsson M.; 1985: *Finite element, modal co-ordinate analysis of structures subjected to moving loads*. J. Sound Vib., **99**, 1-12, doi:10.1016/0022-460X(85)90440-7.

Oral E., Gélis C., Bonilla L.F. and Delavaud E.; 2017: *Spectral element modelling of seismic wave propagation in visco-elastoplastic media including excess-pore pressure development*. Geophys. J. Int., **211**, 1494-1508, doi:10.1093/gji/ggx375.

Park D. and Hashash Y.M.A.; 2004: *Soil damping formulation in nonlinear time domain site response analysis*. J. Earthquake Eng., **8**, 249-274, doi:10.1142/S1363246904001420.

Porsani M.J. and Oliveira S.P.; 2008: *Linearized seismic waveform inversion using a multiple re-weighted least-squares method with QR preconditioning*. Geophys. Prospect., **56**, 61-68, doi:10.1111/j.1365-2478.2007.00662.x.

Porsani M.J., Niwas S. and Ferreira N.R.; 2001: *Robust inversion of vertical electrical sounding data using a multiple reweighted least-squares method*. Geophys. Prospect., **49**, 255-264, doi:10.1046/j.1365-2478.2001.00249.x.

Régnier J., Bonilla L.-F., Bard P.-Y., Bertrand E., Hollender F., Kawase H., Sicilia D., Arduino P., Amorosi A., Asimaki D., Boldini D., Chen L., Chiaradonna A., DeMartin F., Ebrille M., Elgamal A., Falcone G., Foerster E., Foti S., Garini E., Gazetas G., Gélis C., Ghofrani A., Giannakou A., Gingery J.R., Glinsky N., Harmon J., Hashash Y., Iai S., Jeremić B., Kramer S., Kontoe S., Kristek J., Lanzo G., di Lernia A., Lopez-Caballero F., Marot M., McAllister G., Mercerat E.D., Moczo P., Montoya-Noguera S., Musgrove M., Nieto-Ferro A., Pagliaroli A., Pisanò F., Richterova A., Sajana S., Santisi d'Avila M.P., Shi J., Silvestri F., Taiebat M., Tropeano G., Verrucci L. and Watanabe K.; 2016: *International benchmark on numerical simulations for 1D, nonlinear site response (PRENOLIN): verification phase based on canonical cases*. Bull. Seismol. Soc. Am., **106**, 2112-2135, doi:10.1785/0120150284.

Régnier J., Bonilla L.-F., Bard P.-Y., Bertrand E., Hollender F., Kawase H., Sicilia D., Arduino P., Amorosi A., Asimaki D., Boldini D., Chen L., Chiaradonna A., DeMartin F., Elgamal A., Falcone G., Foerster E., Foti S., Garini E., Gazetas G., Gélis C., Ghofrani A., Giannakou A., Gingery J.R., Glinsky N., Harmon J., Hashash Y., Iai S., Kramer S., Kontoe S., Kristek J., Lanzo G., di Lernia A., Lopez-Caballero F., Marot M., McAllister G., Mercerat E.D., Moczo P., Montoya-Noguera S., Musgrove M., Nieto-Ferro A., Pagliaroli A., Passeri F., Richterova A., Sajana S., Santisi d'Avila M.P., Shi J., Silvestri F., Taiebat M., Tropeano G., Vandeputte D. and Verrucci L.; 2018: *PRENOLIN: International benchmark on 1D nonlinear site-response analysis - validation phase exercise*. Bull. Seismol. Soc. Am., **108**, 876-900, doi:10.1785/0120170210.

Santos E. and Bassrei A.; 2007: *L- and ϕ -curve approaches for the selection of regularization parameter in geophysical diffraction tomography*. Comput. Geosci., **33**, 618-629, doi:10.1016/j.cageo.2006.08.013.

Sen M.K. and Stoffa P.L.; 2013: *Global optimization methods in geophysical inversion, 2ⁿᵈ ed*. Cambridge University Press, Cambridge, UK, 302 pp.

Seriani G. and Priolo E.; 1994: *Spectral element method for acoustic wave simulation in heterogeneous media*. Finite Elem. Anal. Des., **16**, 337-348, doi:10.1016/0168-874X(94)90076-0.

Seriani G. and Oliveira S.P.; 2007: *Optimal blended spectral-element operators for forward modeling*. Geophys., **72**, SM95-SM106, doi:10.1190/1.2750715.

Stupazzini M., Paolucci R. and Igel H.; 2009: *Near-fault earthquake ground-motion simulation in the Grenoble valley by a high-performance spectral element code*. Bull. Seismol. Soc. Am., **99**, 286-301, doi:10.1785/0120080274.

U.S. Geological Survey; 2010: *M 5.4 - 20km NNW of Borrego Springs*, CA. <https://earthquake.usgs.gov/earthquakes/eventpage/ci10736069>.

Youd T.L. and Holzer T.; 1994: *Piezometer performance at Wildlife liquefaction site, California*. J. Geotech. Eng., **120**, 975-995, doi:10.1061/(ASCE)0733-9410(1994)120:6(975).

Zeghal M. and Elgamal A.; 1994: *Analysis of site liquefaction using earthquake records*. J. Geotech. Eng., **120**, 996-1017.

*Corresponding author:*     Saulo Pomponet Oliveira
                            Departamento de Matemática, Universidade Federal do Paraná
                            Caixa Postal 19096, CEP 81531-980, Curitiba-PR, Brazil
                            Phone: +55 41 3208-6330; e-mail: saulopo@ufpr.br

## Appendix A: forward modelling and inversion methods

In this appendix we present the details of the forward modelling solution, and the global/local optimization methods used in the inversion.

Let us start with the spatial and temporal discretization of problem (Eq. 1). We have chosen the spectral element method with Gauss-Lobatto-Chebyshev (GLC) collocation points. This numerical method is implicit in time, which gives more flexibility to choose the time step according to the sampling rate, and is able to deliver an accurate solution in coarse and/or irregular grids due to its low dispersion (Seriani and Oliveira, 2007). The method provides an approximation in the form:

$$u_h(z,t) \approx \sum_{j=1}^{N_v-1} u_j(t)\psi_j(z),$$
(A1)

where $\psi_1, \ldots, \psi N_v - 1$ are global Lagrange interpolation shape functions, $N_v = N_e N_p + 1$ is the number of global vertices, and $N_e$ is the number of elements. Replacing Eq. A1 into the Galerkin approximation of Eq. 1, we find the following dynamical equations of motion:

$$\boldsymbol{M}\ddot{\boldsymbol{u}}(t) + \boldsymbol{C}(t)\dot{\boldsymbol{u}}(t) + \boldsymbol{K}(t)\boldsymbol{u}(t) = \boldsymbol{F}(t),$$
(A2)

where

$$M_{i,j} = \int_0^L \rho(z)\psi_j(z)\psi_i(z)\,dz, \quad 1 \le i,j \le N_v - 1, \tag{A3}$$

is the mass matrix,

$$C_{i,j}(t) = \int_0^L \eta(z,t)\psi_{j,z}(z)\psi_{i,z}(z)\,dz, \quad 1 \le i,j \le N_v - 1, \tag{A4}$$

is the simplified, stiffness proportional (Park and Hashash, 2004) viscous damping matrix, and

$$K_{i,j}(t) = \int_0^L G(z,t)\psi_{j,z}(z)\psi_{i,z}(z)\,dz, \quad 1 \le i,j \le N_v - 1, \tag{A5}$$

is the stiffness matrix, whereas $\ddot{u}$, $\dot{u}$, and $u$ are nodal vectors relative to acceleration, velocity and displacement, respectively. The vector $F(t)$ incorporates boundary conditions.

For the time discretization of Eq. A2, we subdivide the interval $[0,T]$ into $N_t$ subintervals $[t_n, t_{n+1}]$ with time step $\Delta t$, $0 \le n \le N_t$, and apply the Newmark method with parameters $\beta = 1/4$ and $\gamma = 1/2$, i.e. the average-acceleration method (Hughes, 1987):

$$\begin{cases} \tilde{u} = u_n + \Delta t v_n + \frac{\Delta t^2}{4}a_n, \\ \tilde{v} = v_n + \frac{\Delta t}{2}a_n, \\ \left(M + \frac{\Delta t}{2}C(t_{n+1}) + \frac{\Delta t^2}{4}K(t_{n+1})\right)a_{n+1} = F(t_{n+1}) - C(t_{n+1})\tilde{v} - K(t_{n+1})\tilde{u} \\ u_{n+1} = \tilde{u} + \frac{\Delta t^2}{4}a_{n+1}, \\ v_{n+1} = \tilde{v} + \frac{\Delta t}{2}a_{n+1}, \end{cases} \tag{A6}$$

where $a_n \approx \ddot{u}(t_n)$, $v_n \approx \dot{u}(t_n)$, and $u_n \approx \ddot{u}(t_n)$. We remark that the average-acceleration method is unconditionally stable (Chopra, 1995; Park and Hashash, 2004) and has been used on dynamic equations with time-dependent matrices (Olsson, 1985).

In the following we briefly review the VFSA algorithm (Ingber, 1989; Sen and Stoffa, 2013) in the simpler setting of a single cooling schedule

$$\mathcal{T}(k) = \mathcal{T}_0 \exp(ck^{1/N}), \tag{A7}$$

where $\tau_0$ and $c$ are the initial temperature and the decay rate, respectively. Let $m^{(0)}$ be a randomly chosen initial guess. For each iteration step $k = 1, 2, \ldots$, we generate $N_r$ samples $u \sim U[0,1]^N$ (i.e. each component of $u$ is drawn from a uniform distribution in $[0,1]$) and define the models $\tilde{m}^{(l)}$ as

$$\begin{aligned} \tilde{m}_i^{(l)} &= \max\left\{m_i^{min}, \min\left\{m_i^{(l)} + y_i(m_i^{max} - m_i^{min}), m_i^{max}\right\}\right\}, \\ y_{i,l} &= sgn(u_{i,l} - 0.5)\mathcal{T}(k)\left[(1 + \mathcal{T}(k)^{-1})^{|2u_{i,l}-1|} - 1\right], \end{aligned} \tag{A8}$$

for $1 \le i \le N$ and $1 \le i \le N_r$. In Eq. A8 we assume the *a priori* bounds $m_i \in [m_i^{min}, m_i^{max}]$ are known. Then, for each $1 \le l \le N_r$, we compute $\Delta E = E(\tilde{m}^{(l)}) - E(m^{(k)})$ and update the model ($m^{(k)} \leftarrow \tilde{m}^{(l)}$) if $\Delta E \le 0$ or if $\Delta E > 0$ and $\exp[-\Delta E/\tau(k)] > r$, where $r \sim U[0,1]$.

The algorithm stops when $E(\boldsymbol{m}^{(k)})$ attains the desired error tolerance or when the temperature $\mathcal{T}(k)$ reaches the minimal prescribed value $\mathcal{T}_f$.

The model obtained with VFSA can be refined by minimizing a quadratic approximation of the misfit function in the neighbourhood of the VFSA solution. Such a minimization can be performed, for instance, with the classical Gauss-Newton method for Eq. 12:

$$\boldsymbol{m}^{(k+1)} = \boldsymbol{m}^{(k)} + \Delta\boldsymbol{m}, \tag{A9}$$

$$\boldsymbol{J}^{(k)}\Delta\boldsymbol{m} = \boldsymbol{d}^{obs} - \boldsymbol{d}(\boldsymbol{m}^{(k)}). \tag{A10}$$

In this method, the update vector $\Delta\boldsymbol{m}$ is found by solving a least squares system involving the $M \times N$ sensitivity matrix $\boldsymbol{J}^{(k)}$, whose entries are given as follows [see, e.g. Björck (1996)]:

$$J_{ij}^{(k)} = \frac{\partial d_i}{\partial m_j}(\boldsymbol{m}^{(k)}) \quad (1 \leq i \leq M, \quad 1 \leq j \leq N). \tag{A11}$$

On the other hand, if the misfit function (Eq. 12) is given in terms of an exponent dependence,

$$E_p^2(\boldsymbol{m}) = \frac{\sum_{n=0}^{N_t}(d_0(t_n) - u_{1,n}(\boldsymbol{m}))^p}{\sum_{n=0}^{N_t} d_0^2(t_n)} + \frac{\sum_{n=0}^{N_t}(v_0(t_n) - v_{1,n}(\boldsymbol{m}))^p}{\sum_{n=0}^{N_t} v_0^2(t_n)} + \frac{\sum_{n=0}^{N_t}(a_0(t_n) - a_{1,n}(\boldsymbol{m}))^p}{\sum_{n=0}^{N_t} a_0^2(t_n)}, \tag{A12}$$

then the update vector is found by solving $\boldsymbol{J}^{p,k}\Delta\boldsymbol{m}^p = \boldsymbol{f}^{p,k}$, where $\boldsymbol{J}^{p,k} = \boldsymbol{W}^{p,k}\boldsymbol{J}^k$, $\boldsymbol{W}^{p,k}$ is a diagonal matrix such that

$$W_{ii}^{(p,k)} = \frac{p}{2}\mathrm{sgn}\left(d_i^{obs} - d_i(\boldsymbol{m})\right)|d_i^{obs} - d_i(\boldsymbol{m})|^{p/2-1} \quad (1 \leq i \leq M), \tag{A13}$$

and $\boldsymbol{f}_i^{(p,k)} = |d_i^{obs} - d_i(\boldsymbol{m})|^{p/2}$ $(1 \leq i \leq M)$. We follow a multiple re-weighted algorithm (Porsani *et al.*, 2001; Porsani and Oliveira, 2008) that defines a set of exponents $\mathcal{P}^{(k)} = \{p_1,...,p_{n_{RW}}\}$ at each inversion step $k$, computing the update vectors $\Delta\boldsymbol{m}^{(i)}$ for each $p_i \in \mathcal{P}^{(k)}$, and selecting the vector $\Delta\boldsymbol{m}$ that minimizes $E(\boldsymbol{m}^{(k)} + \Delta\boldsymbol{m}^{(i)})$.

If $E(\boldsymbol{m}^{(k)} + \Delta\boldsymbol{m}) > E(\boldsymbol{m}^{(k)})$, then we minimize $E(\boldsymbol{m}^{(k)} + \alpha\Delta\boldsymbol{m}^{(i)})$ with $\alpha = 10^{-1}, 10^{-2},..., 10^{-6}$ until $E(\boldsymbol{m}^{(k)} + \alpha\Delta\boldsymbol{m}) \leq E(\boldsymbol{m}^{(k)})$, otherwise, model $\boldsymbol{m}^{(k)}$ is retained and the algorithm stops. This strategy is known as the damped Gauss-Newton method (Björck, 1996). Moreover, we employ the standard Tikhonov regularization

$$\left((\boldsymbol{J}^{(p,k)})^T\boldsymbol{J}^{(p,k)} + \lambda\boldsymbol{I}\right)\Delta\boldsymbol{m} = (\boldsymbol{J}^{(p,k)})^T\boldsymbol{f}^{(p,k)}, \tag{A14}$$

where the regularization parameter $\lambda$ is selected with the $\Theta$-curve (Santos and Bassrei, 2007).

In the numerical experiments, the initial and final temperatures are $\mathcal{T}_0 = 1$ and $\mathcal{T}_f = 0.01$, whereas the parameter $c$ is chosen such that the average rate of change of temperature in log scale is $\Delta\mathcal{T} = 0.01$. With these parameters, the number of VFSA iterations was 460. Moreover, the number of random samples is $N_r = 100$. We use $n_{RW} = 11$ equally-spaced exponents in the WGN algorithm.

## Appendix B: numerical dispersion analysis

In the following we estimate the numerical dispersion of the fully-discrete scheme in Eq. A6. Under the simpler assumptions of homogeneous shear modulus $G_0$ and density $\rho_0$ and absence of loads and damping, the fully-discrete scheme reduces to

$$\left(M_0 + V_0^2 \frac{\Delta t^2}{4} K_0\right) u_{n+1} - 2\left(M_0 - V_0^2 \frac{\Delta t^2}{4} K_0\right) u_n + \left(M_0 + V_0^2 \frac{\Delta t^2}{4} K_0\right) u_{n-1} = 0, \quad \text{(B1)}$$

where $V_0 = (G_0/\rho_0)^{1/2}$ and matrices $M_0$ and $K_0$ are given as

$$(M_0)_{ij} = \int_0^L \psi_i(z)\psi_j(z)\,dz, \quad (K_0)_{ij} = \int_0^L \psi_i'(z)\psi_j'(z)\,dz, \quad \text{(B2)}$$

By substituting into Eq. B1 the vector $u_n$ defined as $u_{n,j} = \exp[-i(w_h t_n - kx_j)]$, we find

$$-4\sin^2\frac{\omega_h \Delta t}{2} M_0 v + \cos^2\frac{\omega_h \Delta t}{2}\Delta t^2 V_0^2 K_0 v \;=\; 0, \quad \text{(B3)}$$

where $v = [\exp(ikx_0),\ldots,\exp(ikx_{Nv-1})]^T$. By taking the Rayleigh quotient approximation in the sense that the residual is orthogonal to , it follows that

$$\sin^2\frac{\omega_h \Delta t}{2} = \frac{\beta}{1-\beta}, \quad \beta = \frac{r^2 h^2}{4N_p^2}\frac{\overline{v}^T K_0 v}{\overline{v}^T M_0 v}, \quad \text{(B4)}$$

where $r = V_0\Delta t N_p/h$ is the Courant number. It is shown in Seriani and Oliveira (2007) that, for an infinite, uniform mesh with element length ,

$$\frac{\overline{v}^T K_0 v}{\overline{v}^T M_0 v} = \frac{4}{h^2}\frac{f(B, N_p, 1/G)}{f(A, N_p, 1/G)}, \quad f(C, N, H) = \sum_{l=0}^N \sum_{j=0}^N C_{l,j}\cos[\pi N H(\xi_j - \xi_l)], \quad \text{(B5)}$$

where $N_p$ is the degree of the spectral element,

$$A_{l,j} = \int_{-1}^1 \hat{\psi}_j(z)\hat{\psi}_l(z)\,dz, \quad B_{l,j} = \int_{-1}^1 \frac{\partial\hat{\psi}_j}{\partial z}(z)\frac{\partial\hat{\psi}_l}{\partial z}(z)\,dz, \quad \text{(B6)}$$

$\hat{\psi}_j(z)$ is the $j$-th Lagrangian shape function of degree $N_p$ satisfying $\hat{\psi}_j(\xi_k) = \delta_{k,j}$, where is the $k$-th GLC collocation point in $[-1, 1]$, and $G = 2\pi N_p/(kh)$ is number of grid points per wavelength. It thus follows that the numerical phase velocity is

$$c_{Ph} = \frac{\omega_h}{\kappa} = \frac{2}{\Delta t\kappa}\sin^{-1}\left(\sqrt{\frac{\beta}{1-\beta}}\right) = \frac{V_0 G}{r\pi}\sin^{-1}\left(\sqrt{\frac{\beta}{1-\beta}}\right). \quad \text{(B7)}$$

In the following we estimate the numerical dispersion of the experiments, recalling that the time step $\Delta t = 0.005$ and the polynomial degree $N_p = 4$. We estimate the Courant number as

$$r \approx \max_{1 \leq e \leq N_e} \frac{V_e \Delta t N_p}{h_e}, \tag{B8}$$

where $V_e$ and $h_e$ are the shear velocity and the length of the *e*-th element, respectively. In the Superstition Hills example, we have $r \approx 7.7$, whereas in the Southern California example we have $r \approx 3$. Fig. B1 shows estimates of the relative phase velocity error $e_{Ph} = (c_{Ph} - V_0)/V_0$ in these cases. It is worth noting that the dispersion error is highly influenced by the time discretization when the Courant number is high. The phase error is below 10% when $G \geq 16$ for $r \approx 3$ and when $G \geq 40$ for $r \approx 7.7$.
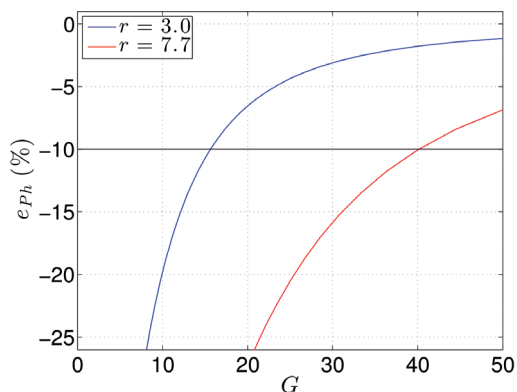


Fig. B1 - Relative phase velocity error of the fully-discrete fourth-degree spectral element method with Courant numbers $r \approx 3$ and $r \approx 7.7$.

In the homogeneous case, we can associate the frequency with the number of grid points per wavelength as follows:

$$f = \frac{V_0 \kappa}{2\pi} = \frac{V_0 N_p}{Gh}. \tag{B9}$$

We estimate the maximum frequency in our experiments as

$$f_{max} \approx \min_{1 \leq e \leq N_e} \frac{V_e N_p}{Gh_e}, \tag{B10}$$

which leads to $f_{max} \approx 7.7$ Hz in WLA and $f_{max} \approx 18.6$ Hz in GVDA, when the number of grid points per wavelength is chosen such that the estimated phase error is at most 10%.

Fig. B2 shows the normalized power spectral density $S(f) = |\hat{d}_0(f)|^2 / max_f\{|\hat{d}_0(f)|^2\}$ of the downhole displacement. The spectral density is negligible at frequencies higher than the maximum frequencies estimated for each example.
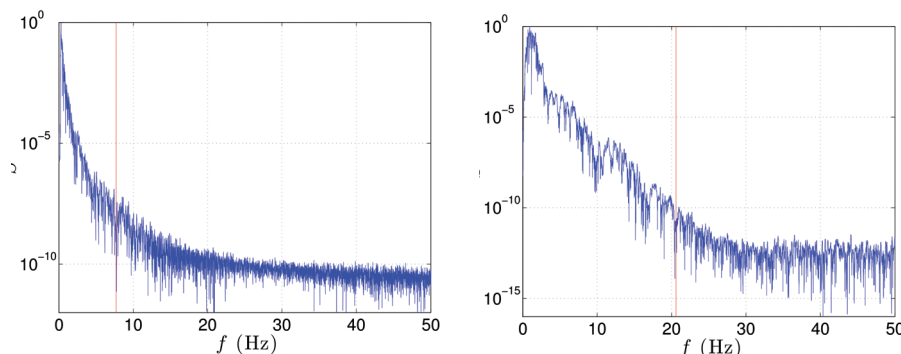


Fig. B2 - Normalized power spectral density of the downhole displacement: WLA (left) and GVDA (right).

## Appendix C: list of symbols

| | |
|---|---|
| $u(z,t)$ | Horizontal displacement ($z$: depth; $t$: time) |
| $\rho(z,t)$ | Density |
| $G(z,t)$ | Shear modulus |
| $\eta(z,t)$ | Viscosity |
| $G_0(z),\ D_0(z)$ | Initial shear modulus and stiffness-dependent damping coefficient |
| $P^\star(z,t)$ | Excess pore-water pressure ratio |
| $d_0(t),\ d_1(t)$ | Recorded surface and downhole horizontal displacement |
| $L$ | Depth of the downhole seismometer |
| $N_l$ | Number of layers in the model |
| $H_l$ | Thickness of the $l$-th layer |
| $\rho_l,\ G_{0,l},\ D_{0,l}$ | Density, initial shear modulus and damping coefficient in the $l$-th layer |
| $P_e^\star(t)$ | Excess pore-water pressure ratio at depth $z=\bar{z}_e$ |
| $G_l(t),\ \eta_l(t)$ | Shear modulus and viscous damping in the $l$-th layer |
| $u_h(z,t)$ | Spectral element approximation of the horizontal displacement |
| $N_p$ | Polynomial degree used in the spectral element method |
| $N_e,\ N_v$ | Number of elements and vertices in the spectral element mesh |
| $T,\ \Delta t,\ N_t$ | Final recording time, time step, and number of time steps |
| $\boldsymbol{u}_n$ | Coefficients of the spectral element solution at time $t_n$ |
| $\boldsymbol{F}_n$ | Nodal vector with boundary conditions at time $t_n$ |
| $\boldsymbol{M},\boldsymbol{C},\boldsymbol{K}$ | Mass, damping, and stiffness matrices |
| $P_i(t)$ | Excess pore-water pressure ratio at the $i$-th observation point |
| $w_{i,e}$ | Weight of $P_i(t)$ in the weighted average that defines $P_e^*(t)$ |
| $\gamma_l$ | $l$-th time-scaling factor of pore-water pressure |
| $G_{0,l}^r$ | Reference shear modulus in the $l$-th layer |
| $N$ | Number of parameters |
| $\boldsymbol{m}$ | Model vector |
| $M$ | Number of observations |
| $\boldsymbol{d}(\boldsymbol{m}),\ \boldsymbol{d}^{obs}$ | Vectors of calculated and observed data |
| $E(\boldsymbol{m})$ | Misfit between predicted and observed data |
| $\mathcal{T}(k)$ | Cooling schedule of the Very Fast Simulated Annealing (VFSA) Algorithm |
| $\mathcal{T}_0,\mathcal{T}_f,\ c$ | Initial/final temperature and temperature decay rate of VFSA |
| $N_r$ | Number of random samples of VFSA |
| $m_i^{min},\ m_i^{max}$ | A *priori* bounds for the $i$-th entry of the parameter vector |
| $\boldsymbol{m}^{(k)}$ | Model vector obtained at the $k$-th iteration |
| $\Delta\boldsymbol{m}$ | Update vector at each inversion step |
| $\boldsymbol{J}^{(k)}$ | Gauss-Newton sensitivity matrix at the $k$-th inversion step |
| $E_p(\boldsymbol{m})$ | Modified misfit function in terms of the exponent $p$ |
| $\boldsymbol{J}^{(p,k)}$ | Sensitivity matrix at the -th inversion step in terms of the exponent $p$ |
| $\boldsymbol{W}^{(p,k)}$ | Weighting matrix in terms of the exponent $p$ |
| $\boldsymbol{f}^{(p,k)}$ | Right-hand side of the weighted least squares system |
| $n_{RW}$ | Number of exponents to evaluate in the multiple re-weighted algorithm |
| $\alpha$ | Step length of the damped Gauss-Newton procedure |
| $\lambda$ | Tikhonov regularization parameter |

| | |
|---|---|
| $\rho_0$, $G_0$, $V_0$ | Density, shear modulus and shear velocity in the homogeneous case |
| $\boldsymbol{M}_0$, $\boldsymbol{K}_0$ | Mass and stiffness matrices in the homogeneous case |
| $\omega_h$, $\kappa$ | Angular frequency and wave number |
| $r$ | Courant number |
| $h$ | Element length in a homogeneous grid |
| $h_e$ | Length of the $e$-th element of an irregular grid |
| $\zeta_k$ | $k$-th Gauss-Lobatto-Chebyshev collocation point |
| $G$ | Number of grid points per wavelength |
| $c_{Ph}$ | Numerical phase velocity |
| $e_{Ph}$ | Phase velocity error |
| $f_{max}$ | Maximum frequency for which the numerical scheme is accurate |
| $S(f)$ | Normalized power spectral density |